# $MoSi_2$-Base Composites

**Mohan G. Hebsur**

**National Aeronautics and Space Administration**

**Glenn Research Center**

**21000 Brookpark Road**

**Cleveland, Ohio 44135**

**Phone: 216–433–3266**

**Email:** mohan.g.hebsur@grc.nasa.gov

## Abstract

Addition of 30 to 50 vol% of $Si_3N_4$ particulate to $MoSi_2$ eliminated its low temperature catastrophic failure, improved room temperature fracture toughness and the creep resistance. The hybrid composite SCS-6/$MoSi_2$-$Si_3N_4$ did not show any matrix cracking and exhibited excellent mechanical and environmental properties. Hi-Nicalon continuous fiber reinforced $MoSi_2$-$Si_3N_4$ also showed good strength and toughness. A new $MoSi_2$-base composite containing in-situ whisker-type $\beta Si_3N_4$ grains in a $MoSi_2$ matrix is also described.

# I. Introduction

Due to high specific strength and stiffness, and the potential for increased temperature capability, composite materials are attractive for subsonic aircraft and future space propulsion systems. Based on high temperature oxidation behavior, it appears that $MoSi_2$ is one of the few intermetallics to have potential for further development. It also has a higher melting point (2296 K) and lower density (6.1 $g/cm^3$) than superalloys, and has electrical and thermal conductivity advantages over ceramics.[1] However, the use of $MoSi_2$ has been hindered due to its brittle nature at low temperatures, inadequate creep resistance at high temperatures, accelerated ('pest') oxidation 773 K, and its relatively high coefficient of thermal expansion (CTE) compared to potential reinforcing fibers such as SiC. The CTE mismatch between the fiber and the matrix results in severe matrix cracking during thermal cycling.

In the last 15 years, an extensive amount of work has been carried out in efforts to improve the high temperature properties of $MoSi_2$ by solid solution alloying, discontinuous reinforcement, and fiber reinforcement. Alloying with refractory metals has improved high temperature creep strength. Substantial improvements in strength have also been achieved by adding particulate, platelets or whiskers of SiC,[2] $TiB_2$, and $HfB_2$.[3] However, the effects of grain refinement may limit the creep strength of these types of composites. To date, $MoSi_2$ alloyed with W and containing 40 vol% SiC has achieved the creep strength superior to that of the superalloys.[4] The addition of SiC whiskers has also yielded improvements in room temperature toughness.

However, it appears that the strength and damage tolerance required for high temperature aerospace applications could only be achieved by reinforcement with high strength continuous fibers.

Maloney and Hecht[5] have done extensive work on the development of continuous fiber reinforced $MoSi_2$-base composites to achieve high temperature creep resistance and room temperature toughness. SiC, sapphire, ductile Mo, and W alloy fibers were investigated. The refractory metal fibers increased both creep strength and fracture toughness, although reaction with the matrix was still a problem. The addition of about 40 vol% of SiC in the form of whiskers and particulate was used to lower the thermal expansion of the $MoSi_2$ base matrix and prevented matrix cracking in the SiC reinforced composites. However, matrix cracking was still observed in an SCS-6 fiber reinforced composite even with the matrix containing up to 40 vol% SiC whiskers. This composite also suffered catastrophic pest attack at 773 K. Sapphire fiber reinforced composites showed no evidence of matrix cracking due to the good thermal expansion match between $MoSi_2$ and $Al_2O_3$. However, the strong fiber-matrix bond did not provide any toughness improvement.

In earlier work[6] of developing $MoSi_2$ suitable for SiC fiber reinforcement, it was found that the addition of about 30 to 50 vol% of $Si_3N_4$ particulate to $MoSi_2$ improved the low temperature accelerated oxidation resistance by forming a $Si_2ON_2$ protective scale and thereby eliminated catastrophic pest failure. The $Si_3N_4$ addition also improved the high temperature oxidation resistance and compressive strength. More importantly, the $Si_3N_4$ addition significantly lowered

the CTE of the $MoSi_2$ and eliminated matrix cracking in SCS-6 reinforced composites even after thermal cycling.[7] The progress made in developing, processing, and characterizing $MoSi_2$-base composites is reported here.

## II. Processing

Several batches containing a mixture of commercially available $MoSi_2$ and either 30 or 50 vol% of $Si_3N_4$ were mechanically alloyed. The $MoSi_2$-$Si_3N_4$ powder was consolidated into "matrix-only" plates by vacuum hot pressing followed by hot isostatic pressing (HIP) to achieve full density. Composite plates of various thickness consisting of 6, 12, or 56 plies of 30 vol% SCS-6 fibers having 0, 0/90 and 90° orientations in a $MoSi_2$-$Si_3N_4$ matrix were prepared by the powder cloth technique and consolidated in the same manner as the material without fibers. This resulted in fully dense material without excessive reaction or damage to the fibers. From the consolidated material, ASTM standard specimens for several tests such as compression, fracture toughness, impact and oxidation were machined by EDM and grinding techniques. Details of the specimen preparation and testing procedures are described elsewhere.

## III. Properties of $MoSi_2$-Base Composites

### *3.1. Microstructure of As-Fabricated Composite*

Figure 1 shows the microstructure of the as-consolidated $MoSi_2$-$Si_3N_4$ matrix. As expected from thermodynamic predictions, the $Si_3N_4$ particles appeared to be quite stable, with very little or no reaction with the $MoSi_2$ even after exposure at 1773 K. X-ray diffraction of $MoSi_2$-$Si_3N_4$ showed only the presence of $MoSi_2$ and a mixture of $\alpha$ and $\beta$ $Si_3N_4$ phases. Even though there is a significant CTE mismatch between $MoSi_2$ and $Si_3N_4$, the small particles of $Si_3N_4$ prevented thermally induced microcracking. As fabricated SCS-6/$MoSi_2$-$Si_3N_4$ composite did not show any matrix cracking. A reaction zone around the fibers was generally 1 micron in thickness and resulted from reaction of the carbon layer to form SiC and $Mo_5Si_3$.[6] The CTE of the matrix and composites plotted as a function of temperature are compared with the monolithic constituents in Figure 2. The addition of $Si_3N_4$ to $MoSi_2$ has effectively lowered the CTE of the matrix, achieving the desired result of eliminating matrix cracking. Furthermore, no cracks were found in either the matrix or the reaction zone even after 1000 thermal cycles between 1473 and 473 K in vacuum. These results show that the use of $Si_3N_4$ was much more effective than SiC.

### *3.2. Oxidation Behavior*

#### *3.2.1. Low Temperature Oxidation*

Figure 3 shows the specific weight gain versus number of cycles at 773 K. Both $MoSi_2$-30 $Si_3N_4$ and $MoSi_2$-50 $Si_3N_4$ show very little weight gain indicating the absence of accelerated oxidation. XRD analysis of both these specimens indicated strong peaks of $Si_2ON_2$ and the absence of $MoO_3$. The $MoSi_2$ exhibited accelerated oxidation followed by pesting.

Figure 4 shows the SCS-6/$MoSi_2$ and SCS-6/$MoSi_2$-30$Si_3N_4$ composites exposed at 773 K. The SCS-6/$MoSi_2$ specimen, which had matrix cracks, was completely disintegrated into powder within 24 cycles, whereas the SCS-6/$MoSi_2$-30$Si_3N_4$ specimen was intact even after 200 cycles. This is again in strong contrast to previous work,[5] where both SCS-6/$MoSi_2$-40 vol% SiC and $Al_2O_3$/$MoSi_2$ composites were reduced to powder after exposure at 773 K. All these observations are consistent with the elimination of pest attack in $MoSi_2$-$Si_3N_4$ composites due to a mechanism involving elimination of the accelerated oxidation associated with a non-protective $MoO_3$ oxide scale. The $Si_2ON_2$ scale forms rapidly, and is protective even at cracks, pores, and interfaces.

### *3.2.2. High Temperature Oxidation*

The results of cyclic oxidation tests at 1473 K, which more closely approximates the conditions under which the material would be subjected in a structural application, are shown in Figure 5. The materials in Figure 5 were subjected to 1 hr heating cycles to 1473 K, followed by 20 minute cooling cycles. The $MoSi_2$-50$Si_3N_4$ particulate composite exhibited superior oxidation resistance as compared to $MoSi_2$ alone. The specific weight gain of $MoSi_2$-50$Si_3N_4$ was only about 1 mg/cm$^2$ in 1000 hr, almost comparable to CVD-SiC, which is considered the best $SiO_2$ former available. The composite initially lost weight due to oxidation of the carbon on the SCS-6 fiber followed by steady weight gain, less than 2 mg/cm$^2$ in 1000 hr. XRD of surface oxides on $MoSi_2$-50 $Si_3N_4$ and hybrid composite indicated strong peaks of $\alpha$-cristobalite.

### *3.3. Mechanical Properties of $MoSi_2$-$Si_3N_4$ Matrix*

#### *3.3.1. Compressive Creep*

Previous work[6,7] showed that the $Si_3N_4$ additions substantially increased compressive strength at all temperatures. This has been augmented with additional testing to further characterize this material. Figure 6 shows the results of constant load compression creep tests at 1473 K on $MoSi_2$-50$Si_3N_4$ plotted as second stage creep rate ($\varepsilon$) versus specific stress. For comparison, several materials such as $MoSi_2$, $MoSi_2$-40SiC,[4] and a single crystal Ni-base superalloy are also included. $MoSi_2$-50$Si_3N_4$ is almost five orders of magnitude stronger than binary $MoSi_2$ and comparable to $MoSi_2$-40SiC. This again confirms the previous observation of beneficial effects of particulate reinforcement. The derived stress exponent, n = 5.3, and the activation energy of 520 kJ/mol calculated from the temperature dependence of creep rate at constant stress, imply a diffusion controlled dislocation mechanism as the rate controlling mechanism.

#### *3.3.2. Fracture Toughness*

The fracture toughness of $MoSi_2$ and $MoSi_2$-$Si_3N_4$ base materials were measured on chevron notched 4 point bend specimens. Figure 7 shows the fracture toughness of $MoSi_2$-50$Si_3N_4$ as a function of temperature. For comparison, results for two monolithic SiC and $Si_3N_4$ are also included. The room temperature fracture toughness of both $MoSi_2$-30$Si_3N_4$ and $MoSi_2$-50$Si_3N_4$

matrix was ~5.2 MPa$\sqrt{m}$, which is about twice the value measured on monolithic $MoSi_2$. Figure 8 also shows that fracture toughness of $MoSi_2$-$Si_3N_4$ increases with temperature, especially beyond 1473 K, which is the BDTT for this material. All of the ceramics maintain the same toughness as temperature is increased.

### *3.3.3. Erosion*

Alman et al.,[9] studied the solid particle erosion behavior of $MoSi_2$-$Si_3N_4$ at room temperature and at elevated temperature. Alumina particles entrained in a stream of nitrogen gas impacted the target material at a velocity of 40 m $s^{-1}$. Impingement angles of either 60, 75 or 90 degrees were used. It was found that the erosion rate for the $MoSi_2$-$Si_3N_4$ composite measured at room temperature was a maximum at the 90 degree incident angle, which is typical of brittle materials. The erosion rate of the composite at 348 K, increased slightly with increasing test temperature up to 973 K, i.e. from 4.1 to 4.9 $mm^3g^{-1}$. At 1173 K, the measured erosion rate decreased to 2.9 $mm^3$ $g^{-1}$. However, at the present time it is unclear if this is a consequence of the $MoSi_2$, phase becoming more ductile at this temperature or is attributable to some other factor. At temperature below 1173 K, the erosion rate of the $MoSi_2$-$Si_3N_4$ composite was similar to that of $\beta Si_3N_4$ and lower than that of Stellite-6B (Figure 8).

## *3.4. Mechanical Properties of SCS-6/$MoSi_2$-$Si_3N_4$ Composite*

### *3.4.1. Fracture Toughness*

Figure 9 shows the load verses displacement plot for SCS-6/$MoSi_2$-30$Si_3N_4$ monolithic chevron notched 4 point bend specimens tested at room temperature. The composite specimen did not break even after testing for 2 hr. The apparent critical stress intensity factor, $K_q$, calculated from the maximum load data was greater than 35 MPa$\sqrt{m}$, which is 7 times tougher than the monolithic material. The toughness of the hybrid composite also increased with temperature reaching as high as 65 MPa$\sqrt{m}$, at 1673 K in argon atmosphere.

### *3.4.2. Tensile Behavior*

Figure 10(a) shows the room temperature tensile stress strain curve for SCS-6/$MoSi_2$-$Si_3N_4$, indicating composite-like behavior; and three distinct regions, an initial linear region, followed by a nonlinear region and a second linear region. The nonlinear region is due to the matrix cracking normal to the loading direction. The second linear region is controlled by fiber strength. Individual SCS-6 fibers were tensile tested at room temperature in the as-received, as-etched and etched-from-composite conditions, and produced average strength values of $3.52 \pm 0.8$, $3.35 \pm 0.6$, and $3.4 \pm 1$ GPa, respectively. Thus, neither etching nor consolidation conditions degraded the strength of the fibers.

Fiber/matrix interfacial properties play an important role in composite mechanical behavior. In the case of this composite system, the carbon layer on SCS-6 provides an appropriate level of

bonding that produces adequate strengthening and toughening. The carbon can react with $MoSi_2$ to form SiC and $Mo_5Si_3$, although the carbon layer is still retained and the reaction zone thickness is not very large at typical HIP temperatures. The fiber matrix interfacial shear strengths determined from a fiber push out test using thin polished sections produced values near 50 MPa, indicating a week bond between the matrix and the fiber.

It was found that the room temperature ultimate tensile strength and strain to fracture were reduced by only 20 percent in a specimen with exposed fibers preoxidized at 1473 K for 200 hr. High temperature tensile tests were performed in air at temperatures up to 1673 K. Figure 10(b) shows the temperature dependence of ultimate tensile strength, along with the data from competitive materials, such as Ni-base single crystal alloy PWA1480 and SCS-6/RBSN. Ni-base single crystal alloy PWA 1480 exhibits higher tensile strength than both $MoSi_2$-base and RBSN-base composites between room temperature and 1273 K; however, PWA 1480 is almost 3 times denser than both composites, and hence is at a disadvantage on a specific strength basis. Figure 10(b) also shows the tensile strength data for the SCS-6 fibers, re-emphasizing the fiber-dominated behavior of the composites. The $MoSi_2$-base composites also exhibited elastic modulus values of ~290/200 GPa between RT and 1473 K.

Several tensile creep tests were carried out on SCS-$6_{[0]}$/$MoSi_2$-$50Si_3N_4$ composite specimens between 1273 and 1473 K in vacuum. Test durations of ~1000 hr were achieved and some idea of long term durability was obtained. Specimens tested at these temperatures exhibited a short

primary creep stage and an extended secondary stage. The minimum creep rates ranged from $1.0\times10^{-9}$ to $2.0\times10^{-9}$ $s^{-1}$ at 70 MPa between 1373 and 1473 K.

### *3.4.3. Impact Behavior*

The Charpy V-notch (CVN) impact tests were conducted on full size specimens of $MoSi_2$-$50Si_3N_4$ matrix and SCS-$6_{[0]}$ and $_{[0/90]}$ oriented /$MoSi_2$-$50Si_3N_4$ hybrid composites between liquid nitrogen temperature (77 K) and 1673 K in air. Figure 11(a) shows the force time curves obtained from the instrumented impact tests at room temperature for monolithic $MoSi_2$-$50Si_3N_4$, SCS-$6_{[0]}$ and $_{[0/90]}$/$MoSi_2$-$50Si_3N_4$ composites. The maximum value of force represents the elastic energy required for crack initiation. The hybrid composite in [0] orientation exhibited the highest peak force values, followed by the cross-plied and finally the monolithic material. At 1673 K, the peak force values for all three materials were higher than their corresponding values at room temperature. The hybrid composite exhibited a gradual, stepwise decrease in load after the peak force was achieved. This indicates substantial energy absorption during crack propagation, and was especially pronounced in the [0] orientation.

Figure 11(b) shows the temperature dependence of CVN energy for $MoSi_2$-base materials compared with other potential materials such as superalloys, and ceramics. The CVN energy for both the monolithic $MoSi_2$-$50Si_3N_4$ and the hybrid composites increased with increasing temperature. The fiber reinforcement in [0] orientation increased the impact resistance by 5 times

and in [0/90] orientation nearly two times. The CVN energy of SCS-6/$MoSi_2$-50$Si_3N_4$ was comparable to the cast superalloy B-1900 but substantially lower than the wrought superalloy Hastelloy X. The CVN energy of $MoSi_2$-50$Si_3N_4$ monolithic was comparable to Mo alloys and in-situ toughened $Si_3N_4$ (AS-800) and was far superior to NiAl, and monolithic hot pressed $Si_3N_4$, and SiC. Unlike $MoSi_2$-50$Si_3N_4$ which shows increased CVN energy with temperature (beyond 1273 K), the AS-800 shows a constant CVN energy between 77 and 1673 K. The monolithic SiC shows a slight decrease of CVN energy with temperature. This is probably due to the degradation caused by densification aids used with SiC.

### *3.5. Hi-Nicalon/$MoSi_2$-$Si_3N_4$ Composite*

Most of the attractive strength and toughness values reported so far were achieved with composites reinforced with SCS-6 fibers. This fiber does not have adequate creep strength at the highest temperatures envisioned for $MoSi_2$ and is too large to be bent around the sharp radii needed to make complex shapes. Finer diameter fibers are preferred on a cost, shape making, creep resistance, and toughness basis. Hi-Nicalon is the best currently available fiber, although Dow Corning's Sylramic® fiber, is also appropriate for this $MoSi_2$-$Si_3N_4$ matrix. A transition in effort to Hi-Nicalon fibers was therefore investigated, first using tow fibers that are spread out, wound on a drum and then infiltrated with matrix powder and ultimately woven cloth.

Tape casting was adopted as a powder metallurgy method for composite fabrication. Initially, several casting trials of $MoSi_2$-$Si_3N_4$ were carried out to optimize various parameters such as particle size, type and amount of binder and solvent, flow behavior of the slurry, and binder burn-out cycle. A 56 ply composite of SCS-6/$MoSi_2$-$Si_3N_4$ was successfully fabricated by tape casting followed by the standard hot press plus HIP consolidation. Composites with small diameter fibers such as SCS-9 (75 μm) and coated Hi-Nicalon (18 to 20 μm) were successfully fabricated.[8]

### *3.6. Mechanical Properties of Hi-Nicalon/$MoSi_2$-$Si_3N_4$ Composite*

The influence of fiber diameter and architecture on mechanical properties was investigated by conducting room temperature tensile and fracture toughness tests on specimens of SCS-6, SCS-9 and BN/SiC coated Hi-Nicalon/$MoSi_2$-50$Si_3N_4$ hybrid composite. Testing in the [0] direction (longitudinal) produced the highest strength, (700 to 1000 MPa strength and 1.2 percent total strain) to failure. Testing in the [90] direction produced the lowest ultimate tensile strength of only 72 MPa and 0.04 percent strain to failure for SCS-6 reinforced composite. This is not an unexpected result since the fibers cannot bridge matrix cracks in the transverse direction, and cross-plied laminates or woven two or three dimensional architectures are required to achieve more isotropic properties. For example, the Hi-Nicalon reinforced composite exhibited high strength and strain to failure in the 0/90 architecture, about 60 percent of the unidirectional value, Figure 12(a). Figure 12(b) shows that the Hi-Nicalon/$MoSi_2$-$Si_3N_4$ in [0/90] direction exhibited

higher fracture toughness than the CMC's Hi-Nicalon/SiC and Hi-Nicalon/$Si_3N_4$, even though they were tested in the more favorable [0] direction.[10] The CMC's were processed at much higher temperatures, 1873 to 2073 K, causing more fiber degradation than Hi-Nicalon/$MoSi_2$-$Si_3N_4$ and therefore exhibited lower toughness.

Figure 13 shows the influence of fiber diameter and architecture on flexural stress rupture at 1473 K/210 MPa in air. This figure clearly indicates the limited improvement with large diameter fiber and more than two orders of improvement with fine diameter fiber [0/90 oriented] in stress rupture lives.

### *3.7: 2D Hi-Nicalon/$MoSi_2$-$Si_3N_4$ Composite by Melt Infiltration*

In order to respond to the industrial need of low cost processing of complex shaped $MoSi_2$-base composites, it was decided to initiate the melt infiltration processing of two-dimensional woven Hi-Nicalon preforms. This kind of processing is being used for SiC/SiC composites. The preforms 10×15×0.3 cm and having a dual layer coating of BN and SiC by chemical vapor infiltration were obtained from DuPont and cut into of 1.2 cm wide × 15 cm long strips. These strips were placed in a Plaster of Paris mold. A water based slurry of $MoSi_2$-$Si_3N_4$ mixture was vacuum infiltrated into the strips. About 50 vol% infiltration was achieved using this technique. The slurry infiltrated pre-forms were dried and then infiltrated with molten silicon alloy to

achieve full density. Preliminary results on microstructure and mechanical property of the melt infiltrated composites are promising.

### *3.8. Applications of $SiC/MoSi_2$-$Si_3N_4$ Composite*

The hybrid composite tested for blade outer airseal component (BOAS) in the aggressive environment of gas turbine engine. Two engine test coupons of the $BN/Si_3N_4$ coated Hi-Nicalon$_{[0/90]}$ /$MoSi_2$-50$Si_3N_4$ hybrid composite were made according to Pratt and Whitney's design. After machining, the surfaces of these coupons were coated with 2 μm thick by CVD-SiC to protect the exposed fibers from environmental degradation. These coupons were tested in Pratt and Whitney's demonstrator engine, XTC/66/b, to simulate (BOAS) thermal cyclic conditions. One surface of the test coupon was facing the jet fueled flame, which reached approximately 1478 K and produced a thermal gradient of about 873 K between the exposed (front) and unexposed (back) surfaces. This hybrid composite performed significantly better than a SiC whisker reinforced $MoSi_2$, which showed severe cracking within the first few cycles. The hybrid composite was removed after 15 cycles and post-test examination did not reveal any surface or matrix cracking. The other applications of this hybrid composite include exhaust nozzle and combuster components of a gas turbine engine.

## IV. $MoSi_2$-β$Si_3N_4$ Composite

However, manufacturing of state-of-the-art fiber-reinforced composite is still quite expensive due to the high cost of fibers and fiber coatings. This problem can be alleviated by reinforcing a $MoSi_2$-base alloy with a high volume fraction of randomly oriented, in-situ grown, long whisker-type grains of $\beta Si_3N_4$. This engineered microstructure is produced through proper thermomechanical treatment and the use of sintering additives, which promote the growth of long whiskers of $\beta Si_3N_4$ in a fully dense $MoSi_2$ matrix. The combination of properties achieved by this new alloy would make it a viable alternative to continuous fiber reinforced composite.

### *4.1. Processing*

A series of processing runs, summarized in table I, were made in order to determine the minimum requirements necessary to produce a fully dense material with the desired in-situ toughened microstructure composed of whisker-like $Si_3N_4$ grains. From the consolidated material, specimens for determining physical, mechanical, and environmental properties were machined using EDM. Details of the processing, specimen design and testing procedures are described elsewhere.[11]

### *4.2. Microstructure*

Figure 14(a) shows SEM back scattered image of a fully dense $MoSi_2$-$\beta Si_3N_4$ composite (MS-70). During processing, the original $\beta Si_3N_4$ powder particles are transformed into randomly oriented whiskers of $\beta Si_3N_4$. These long whiskers are well dispersed throughout the material and

appear to be quite stable, with very little or no reaction with the $MoSi_2$, even at 2173 K. Figure 14(b) shows a back-scattered image of $MoSi_2$-$\beta Si_3N_4$ (MS-80) with the $\beta Si_3N_4$ exhibiting the blocky aggregate type morphology.

### *4.3. Physical Properties*

Density of the in-situ toughened $MoSi_2$-$\beta Si_3N_4$ (alloy MS-70) was measured to be 4.57 ± 0.01 g/cm$^3$, Vickers microhardness was 10.7 ± 0.6 GPa, and average CTE was about 4.0 ppm/K. Figure 15 shows the dynamic Young's Modulus for two batches of $MoSi_2$-$\beta Si_3N_4$ (MS-70 and MS-80) as a function of temperature. Young's Modulus for MS-70 decreases with increasing temperature but only by about 10 percent over a 1273 K range. As expected, the denser alloy (MS-70) exhibits a higher modulus at all temperatures compared to MS-80, which contained residual porosity after processing.

### *4.4. Electrical Conductivity*

Electrical conductivity is a very important property in determining whether a material can be suitably machined by EDM. Room temperature electrical conductivity of various $MoSi_2$-base materials and $Si_3N_4$ ceramic were measured on rectangular bars. $MoSi_2$-$\beta Si_3N_4$ (MS-70) composite showed more than an order of magnitude higher (20/ohm.com) conductivity for the

$MoSi_2$-$\beta Si_3N_4$ compared to AS-800 (0.5/ohm.com). Both the $MoSi_2$ and $MoSi_2$-$\beta Si_3N_4$ have proven machineable by EDM. In contrast, AS-800 cannot be EDM'ed.

### *4.5. Mechanical Properties*

#### *4.5.1. Compression Strength*

The compression yield strengths of (MS-80) measured between room temperature and 1673 K are shown in Figure 16. For comparison the compression strengths of $MoSi_2$-$\beta Si_3N_4$ (MS-50) are also included. Both materials contain 50 vol% of $Si_3N_4$ but $MoSi_2$-$\beta Si_3N_4$ has higher strength than $MoSi_2$-$\beta Si_3N_4$ at all temperatures. Furthermore, the MS-80 material has less than optimum microstructure and it would be anticipated that the in-situ toughened MS-70 or MS-60 material would exhibit even better strength, especially at high temperatures.

#### *4.5.2. Fracture Toughness*

A summary of the fracture toughness values for in-situ toughened $MoSi_2$-$\beta Si_3N_4$ (MS-70) determined by four different test methods is presented in table II. The SEVNB method yielded the fracture toughness (7.4 MPa$\sqrt{m}$) and the CNB method resulted in the highest value (12.2 MPa$\sqrt{m}$). A few CNB specimens machined from MS-60 exhibited even higher fracture toughness of 14.5 MPa$\sqrt{m}$. The SEVNB method tends to provide a lower value of fracture

toughness presumably due to rising R-curve behavior.

It is worth comparing the fracture toughness between $MoSi_2$-$\beta Si_3N_4$ (MS-70) and $MoSi_2$-$\beta Si_3N_4$ (MS-40 and MS-50). The $\beta Si_3N_4$ reinforced materials exhibited $K_{Ic}$ values of 3.5 ± 0.4 MPa$\sqrt{m}$ and 4.9 ± 0.3 MPa$\sqrt{m}$ for MS-40 and MS-50, respectively compared to 8.9 ± 0.5 MPa$\sqrt{m}$ for the in-situ toughened MS-70, as determined by the SEPB method. Therefore, a significant increase in fracture toughness, up to 157 percent by SEPB method, was achieved for MS-70 material through improved material processing and engineered microstructural control. In addition, the fracture toughness of the MS-70 material was greater than that (7.2 ± 0.2 MPa$\sqrt{m}$), of AS-800, an in-situ toughened $Si_3N_4$. Figure 17 shows a comparison of the indent crack trajectories generated in the polished surfaces of MS-40, MS-50, and MS-70 materials. Indents were made with a Vickers indenter using an indent load of 98 N. The length of crack eminated from the indent corner was significantly shorter for the MS-70 material, illustrating again that fracture resistance (hence, fracture toughness) was much greater than the MS-40 and MS-50 materials. Also note the more tortuous path of the crack for the MS-70 material.

### *4.5.3. Flexural Strength and Weibull Behavior*

Figure 18 shows a comparison of the four-point flexural strength of $MoSi_2$-$\beta Si_3N_4$ (MS-70), and $MoSi_2$-$\beta Si_3N_4$ (MS-50) and AS-800 as a function of temperature up to 1673 K. AS-800 is

stronger by about 10 percent than $MoSi_2$-$\beta Si_3N_4$ (MS-70) at all temperatures. Figure 18 also shows that the in-situ whisker reinforced $MoSi_2$-$\beta Si_3N_4$ (MS-70) is significantly stronger than $MoSi_2$-$\beta Si_3N_4$ (MS-50) at all temperatures. Room temperature four point bend tests were carried out to measure the strength and Weibull modulus of two types $MoSi_2$-$\beta Si_3N_4$ materials, one with the $\beta Si_3N_4$ in a whisker-like morphology (MS-70) and the other with a more characteristic blocky $\beta Si_3N_4$ particulate structure (MS-80). The resulting Weibull distributions for MS-70 and MS-80 are plotted in Figure 19. The in-situ toughened material (MS-70) exhibits a much higher characteristic strength and Weibull modulus (728 MPa and m = 17) than the MS-80 material (461 MPa and m = 9.8).

The toughening mechanisms operative in the in-situ whisker reinforced $MoSi_2$-$\beta Si_3N_4$ are crack deflection, crack bridging, and grain pull-out. Through a combination of these three toughening mechanisms the in-situ whisker reinforced $MoSi_2$-$\beta Si_3N_4$ exhibited significant toughness compared to materials of similar composition. In both the $MoSi_2$-$\beta Si_3N_4$ (MS-50 and MS-40) and the MS-80 material, the $Si_3N_4$ did not possess a whisker structure and hence these materials only underwent crack deflection resulting in a lower fracture toughness. Furthermore, because the additional toughening mechanisms, such as bridging and pullout, lead to a rising R-curve behavior, the in-situ whisker reinforced $MoSi_2$-$\beta Si_3N_4$ would be expected to have better reliability. Because the results do indicate a higher Weibull modulus and strength for MS-70 compared to other $MoSi_2$-base materials, then either the flaw population in this material is unusually uniform or a

rising R-curve behavior is active during fracture. Another consequence of R-curve behavior would be discrepancies in fracture toughness values obtained from the different testing techniques as summarized in table II.

### 4.6 Environmental Resistance

#### *4.6.1 Low Temperature Oxidation and Pesting*

Figure 20 shows specific weight gain versus number of cycles at 773 K for $MoSi_2$-$\beta Si_3N_4$ (MS-70) and binary $MoSi_2$. The oxidation behavior of a MoSiB[13] alloy (at.% 84.5Mo-6.5Si-8B-1Hf) is also included for comparison. $MoSi_2$-$\beta Si_3N_4$ (MS-70) shows very little weight gain compared to binary $MoSi_2$ and the MoSiB alloy, indicating the absence of accelerated oxidation. In contrast, the binary $MoSi_2$ and MoSiB alloys exhibited accelerated oxidation followed by pesting. XRD analysis of the $MoSi_2$-$\beta Si_3N_4$ specimen indicated strong peaks of $Si_2ON_2$ and the absence of any $MoO_3$.

#### *4.6.2. High-Temperature Cyclic Oxidation*

Cyclic oxidation tests were carried out on rectangular coupons of the in-situ toughened $MoSi_2$-$\beta Si_3N_4$ (MS-70) at 1273 and 1623 K in air for about 100 cycles where each cycle consisted of 1 hr heating followed by 20 minutes of cooling. The material exhibited a parabolic oxidation behavior with weight gain of only 0.03 and 0.4 $mg/cm^2$ at 1273 and 1623 K, respectively. These

weight gain values are smaller than those for AS-800 (0.06 and 0.63 at 1273 and 1623 K, respectively). XRD analysis of the oxidized surface of the in-situ toughened $MoSi_2$-$\beta Si_3N_4$ indicated strong peaks of $\alpha$ cristobalite.

## 4.7 Applications of $MoSi_2$-$\beta Si_3N_4$ Composite

The mechanical properties of $MoSi_2$-based composites are now adequate for a wide range of industrial and military applications. A few of the potential applications are high lighted below.

### *4.7.1. Diesel Engine Glow Plug*

$MoSi_2$-$Si_3N_4$ diesel engine glow plug for automotive applications has recently been developed. This glow plug has significant advantages for automotive diesel engines. It possesses a long glow plug lifetime (13 years) in the diesel fuel combustion environments. It also produces higher heating rates than metal glow plugs, allowing for faster starting of the diesel engine by approximately a factor of two. The glow plug is microstructurally tailored $MoSi_2$-$Si_3N_4$ composite which contains approximately 30 vol% $MoSi_2$ in a $Si_3N_4$ matrix. It is composed of a core and a sheath both of which have the same phase, but with different $MoSi_2$ morphology. The core has an interconnected $MoSi_2$ phase so is electrically conductive, while the sheath has a non-interconnected $MoSi_2$ phase so it is electrically insulating. Since both the core and sheath are essentially the same composite composition except for phase interconnectivity, there is perfect

match of thermal expansion coefficients and material compatibility.

### *4.7.2. Aircraft Engines*

Industrial applications typically require fracture toughness values of 10 MPa$\sqrt{m}$, while aerospace applications require 15 MPa$\sqrt{m}$ or higher. The fracture toughness of $MoSi_2$-$\beta Si_3N_4$ is very close to 15 MPa$\sqrt{m}$ making this ideal for blade outer air seal component in an aircraft engine. The low cost of manufacturing near-net shape component and other beneficial properties such as ease of machining by EDM technique of $MoSi_2$-$\beta Si_3N_4$ makes this an attractive material in aerospace applications.

## V. Concluding Remarks

A wide spectrum of mechanical and environmental properties have been measured in order to establish feasibility of an SiC/$MoSi_2$-$Si_3N_4$ hybrid composite. The high impact resistance of the composite is of particular note, as it was a key property of interest for engine applications. Processing issues have also been addressed in order to lower cost and improve shape making capability. The composite system remains competitive with other ceramics as a potential replacement for superalloys. However, the cost of fiber, fiber coating and the processing is a major concern. Therefore a new $MoSi_2$-based composite with an engineered microstructure consisting of large particles of $MoSi_2$ reinforced with long whisker-shaped grains of $Si_3N_4$ was

developed. This in-situ toughened $MoSi_2$-$\beta Si_3N_4$ exhibited higher fracture toughness and Weibull modulus than other $MoSi_2$-base materials or a structural $Si_3N_4$ ceramic. This material also exhibits excellent resistance to intermediate temperature pesting that affects most other Mo-base and $MoSi_2$-base alloys. Given this combination of good fracture resistance and excellent environmental resistance, the in-situ toughened $MoSi_2$-$\beta Si_3N_4$ shows great promise as a high temperature structural material. However, the development of reliable processing methods will be needed to broaden interest in this material.

## References


[1]A.K. Vasudevan and J.J. Petrovic, "Key Development in High Temperature Structural Silicides," Mat. Sci. & Eng, **A261,** [1–2] 1–5, (1999).

[2]S. Bose, "Engineering Aspect of Creep Deformation of Molybdenum Disilicide," in "High Temperature Silicides," Eds., A.K. Vasudevan and J.J. Petrovic. North Holland, NY, 217–225 (1992).

[3]R.M. Aikin, Jr., "High Temperature Mechanical Behavior of Discontinuously Reinforced $MoSi_2$ Composites," Structural Intermetallics, Eds. R. Darolia, J.J. Lewandowski, C.T. Liu, D.B. Miracle, and M.V. Nathal, TMS, Warrendale, PA, 791–798 (1993).

[4]K. Sadananda, C.R. Feng, and H. Jones, "Creep of Molybdenum Disilicide" in "High Temperature Silicides." Eds., A.K. Vasudevan and J.J. Petrovic. North Holland, NY, 227–237 (1992).

[5]M.J. Maloney and R.J. Hecht, "Development of continuous Fiber-Reinforced $MoSi_2$-base Composites," in High Temperature Silicides, Eds., A.K. Vasudevan and J.J. Petrovic, North Holland, NY, 19–32 (1992).

[6]M.G. Hebsur, "Pest resistant and Low CTE $MoSi_2$-Matrix for High Temperature Structural Applications," in "Intermetallic Matrix Composites III," Eds., J.A. Graves, R.R. Bowman, and J.J. Lewandowski, MRS Proc. **350**, [4–6], MRS, Pittsburgh, PA, 177–182 (1994).

[7]M.G. Hebsur, "Pest resistant $MoSi_2$ Materials and Method of Making," U.S. Patent, #5,429,997, (1995).

[8]M.G. Hebsur, "Development and Characterization of $SiC_{(f)}MoSi_2$-$Si_3N_{4(p)}$ Hybrid Composites," Mater., Sci. & Eng., **A261**, [1–2] 24–37, (1999)

[9]D.E. Alman, J.H. Tylczak, J.A. Hawak, and M.G. Hebsur, "Solid Particle Erosion Behavior of an $Si_3N_4$-$MoSi_2$ Composite at Room and Elevated Temperatures," Mat., Sci., & Eng., **A261,** [1–2] 245–251 (1999).

[10]Knakano, K. Sasaki, M. Fujikura, and H. Ichikawa, "SiC-and $Si_3N_4$-Matrix Composites According to the Hot-Pressing Route" in "High Temperature Ceramic-Matrix Composites II," "Manufacturing and Materials Development," Eds., A.G. Evans and R. Nasalin, American Ceramic Society, Westerville, OH, 215–229 (1995).

[11]M.G. Hebsur, S.R. Choi, J.D. Whittenberger, J.A. Salem, and R.D. Noebe, "Development of Tough, Strong and Pest Resistant $MoSi_2$-$\beta Si_3N_4$ Composites for High Temperature Structural Applications," in "Structural Intermetallics," Eds., K.J. Hemker, D.M. Dimiduk, H. Clemens, R. Darolia, H. Inui, V.K. Sikka, M. Thomas, and J.D. Whittenberger, TMS, Warrendale, PA, 745–753 (2001).

[12]S.R. Choi, and M.G. Hebsur, "Elevated Temperature Slow Crack Growth and Room Temperature Fracture Toughness of $MoSi_2$-$50Si_3N_4$ Composites," *Ceram. Eng. Sci. Proc.*, **19,** [3] 361–369 (1998).

[13]D.M. Berczik, "Oxidation Resistant Molybdenum Alloy," U.S. Patent, No. 5,696,150 (1997).

## Figure captions

Figure 1.—SEM micrograph of consolidated $MoSi_2$ -$50Si_3N_4$. $MoSi_2$ is the light phase.

Figure 2.—Thermal expansion data for several $MoSi_2$-base materials and SiC reinforcing phase.

Figure 3.—Specific weight versus number of cycles for various $MoSi_2$-base materials cyclic oxidized at 773 K in air.

Figure 4.—SCS-6 fiber reinforced specimens cyclic oxidized at 773 K in air. (a) $MoSi_2$ matrix after 24 cycles. (b) $MoSi_2$-$30Si_3N_4$ matrix after 200 cycles.

Figure 5.—Specific weight gain versus number of cycles plot for $MoSi_2$-$50Si_3N_4$ monolithic and SCS-6/ $MoSi_2$-$50Si_3N_4$ hybrid composite cyclic oxidized at 1523 K in air.

Figure 6.—Second stage creep rate versus specific stress at 1473 K for $MoSi_2$-$50Si_3N_4$ compared with other materials.

Figure 7.—Temperature dependence of fracture toughness of $MoSi_2$-base materials compared with ceramic matrices.

Figure 8.—Effect of test temperatures on the erosion rate at a fixed impingement angle of 75°.

Figure 9.—Load-time curves from a chevron notched 4 point bend specimens of SCS-6/$MoSi_2$-$50Si_3N_4$ and $MoSi_2$-$50Si_3N_4$ tested at room temperature.

Figure 10(a).—Room temperature tensile stress-strain curves for 6-ply SCS-6/$MoSi_2$-$Si_3N_4$ hybrid composites.

Figure 10(b).—Temperature dependence of ultimate tensile strength of 6-ply SCS-6/$MoSi_2$-$50Si_3N_4$ base composites compared with other materials.

Figure 11(a).—Force-time curves for $MoSi_2$.$Si_3N_4$ monolithic and SCS-6/$MoSi_2$-$Si_3N_4$ hybrid composites obtained from the instrumented Charpy impact tests at room temperature.

Figure 11(b).—CVN energy versus temperature plot for $MoSi_2$-base composites compared with other materials.

Figure 12.—Influence of fiber diameter and orientation on room temperature. (a) Tensile strength. (b) Fracture toughness of $MoSi_2$-base hybrid composites.

Figure 13.—Influence of SiC fiber diameter and orientation on flexural stress rupture of $MoSi_2$-$50Si_3N_4$ at 1473 K/210 MPa.

Figure 14(a).—SEM back scattered image of $MoSi_2$-$\beta Si_3N_4$ (MS-70) showing randomly oriented in-situ grown long whiskers of $\beta Si_3N_4$ and large $MoSi_2$ particle size. (b) SEM back scattered image of $MoSi_2$-$\beta Si_3N_4$ (MS-80) where the $Si_3N_4$ has a blocky particulate structure and not a whisker-like morphology.

Figure 15.—Dynamic Young's Modulus versus temperature for $MoSi_2$-$\beta Si_3N_4$ materials. MS-70 and MS-80.

Figure 16.—Compressive yield strength versus temperature for two $MoSi_2$-$Si_3N_4$ alloys.

Figure 17.—Indentation crack length and trajectories for $MoSi_2$-50%, $Si_3N_4$. (a) MS-40. (b) MS-50. (c) MS-70. An Indent load of 98 N was applied to initiate the cracks.

Figure 18.—Flexural strength as a function of temperature for $MoSi_2$-$\beta Si_3N_4$ (MS-70) compared to AS-800 and $MoSi_2$-$Si_3N_4$ (MS-50).

Figure 19.—Weibull (flexure) strength distribution for $MoSi_2$-$\beta Si_3N_4$ (MS-70) and (MS-80) materials.

Figure 20.—Specific weight gain versus number of cycles of $MoSi_2$-$50\beta Si_3N_4$ (MS-70) at 773 K compared with $MoSi_2$ and MoSiB alloy.

Table I.—Processing Conditions for the Various Alloys Investigated

| Alloy designation | Alloy composition, wt% | Consolidation conditions | Microstructure |
|---|---|---|---|
| MS-60 | $MoSi_2$-35$Si_3N_4$-4$Al_2O_3$-1$Y_2O_3$ | Hot Press: 1673 K/120 MPa/2-hrs<br>HIP (Ta can): 2173 K/300 MPa/2-hrs | Fully dense $\beta Si_3N_4$ with long whisker-type morphology |
| MS-70 | $MoSi_2$-35$Si_3N_4$-4$Al_2O_3$-1$Y_2O_3$ | Hot Press: 2073 K/70 MPa/3-hrs<br>HIP (no can necessary): 2173 K/300 MPa/2-hrs | Fully dense $\beta Si_3N_4$ with long whisker-type morphology |
| MS-80 | $MoSi_2$-35$Si_3N_4$-4$Al_2O_3$-1$Y_2O_3$ (Processed in 01-HD attritor with significant powder loss) | Hot Press: 1873 K/56 MPa/2-hrs + 1973 K/56 MPa/2-hours<br>HIP (graphoil wrap): 2173 K/280 MPa/2-hrs | Not fully dense $\beta Si_3N_4$ with blocky morphology |
| MS-50 | $MoSi_2$-35$Si_3N_4$ | Hot Press: 1673 K/120 MPa/2-hours<br>HIP (Ta can): 1773 K/300 MPa/2-hrs | Fully dense $\beta Si_3N_4$ with blocky morphology |
| MS-40 | $MoSi_2$-35$Si_3N_4$ | Hot Press: 1473 K/200 MPa/2-hrs<br>HIP (Ta can): 1473 K/280 MPa/2-hrs. | Not fully dense Fine grained $MoSi_2$ and blocky $\beta Si_3N_4$ |

Table II .—Fracture Toughness of MS-70 Determined at Room Temperature by Four Different Test Methods

| Test method | Conditions | Fracture toughness, $K_{IC}$ (MPa$\sqrt{m}$) |
|---|---|---|
| Indentation Fracture (IF) | 5 indents at 98N and 196 N | 9.4 ± (0.5)[b] |
| Single Edge V-Notched Beam (SEVNB) | Three specimens used; $\alpha = 0.25$[a] | 7.4 ± (0.4)[b] |
| Single Edge Precracked Beam (SEPB) (ASTM C1421) | Three specimens used; $\alpha = 0.4$ to 0.6[a] | 8.9 ± (0.5)[b] |
| Chevron-Notched Beam (CNB) (ASTM C1421) | Average of five specimens | 12.2 ± 0.2 |

[a]Indicates the ratio of precrack size to specimen depth.
[b]Indicates ± 1.0 standard deviation.

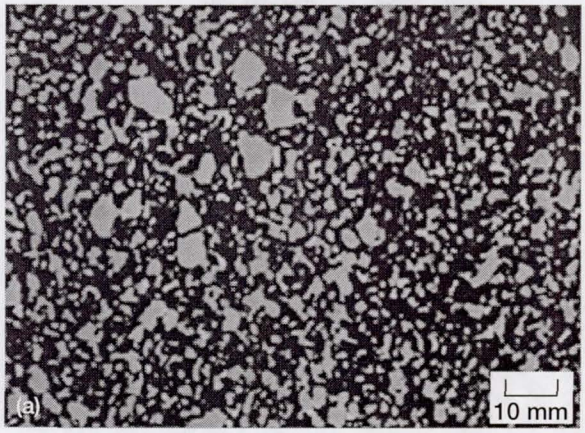


Figure 1

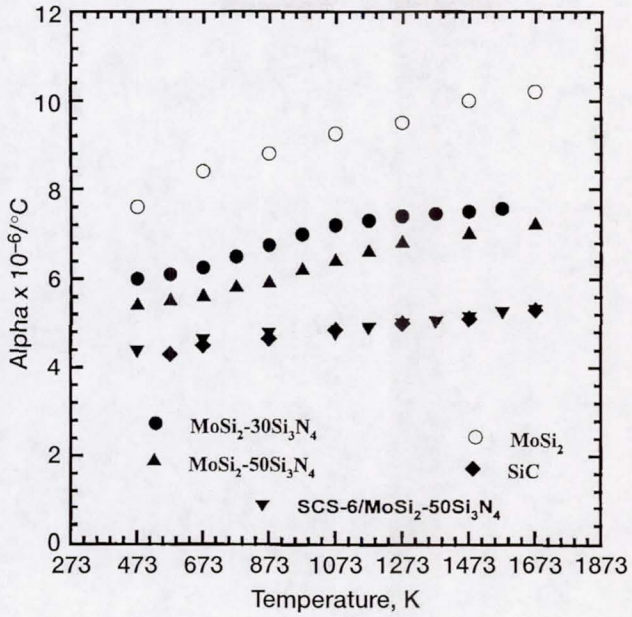
12
10
8
6
4
2
0
Alpha x 10-6/°C
273
473
673
873
1073
1273
1473
1673
1873
Temperature, K
MoSi2-30Si3N4
MoSi2-50Si3N4
MoSi2
SiC
SCS-6/MoSi2-50Si3N4

Figure 2

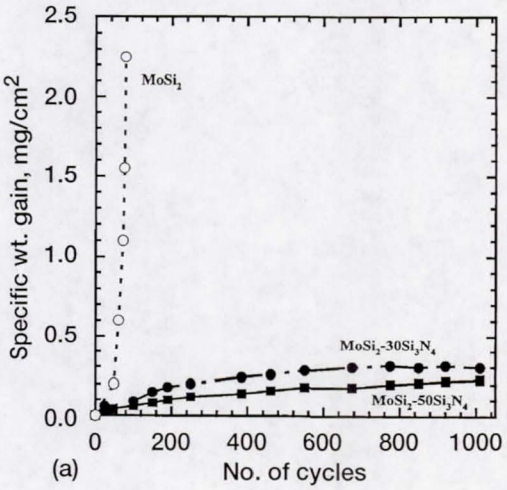
2.5
2.0
1.5
1.0
0.5
0.0
Specific wt. gain, mg/cm2
MoSi2
MoSi2-30Si3N4
MoSi2-50Si3N4
0
200
400
600
800
1000
No. of cycles
(a)

Figure 3

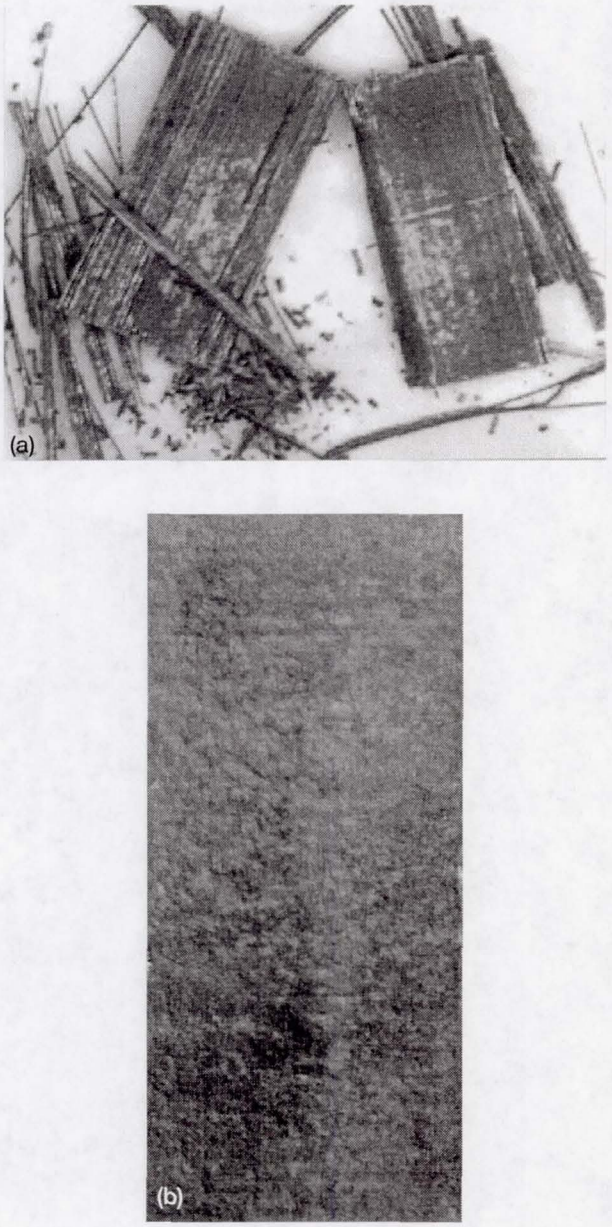


Figure 4

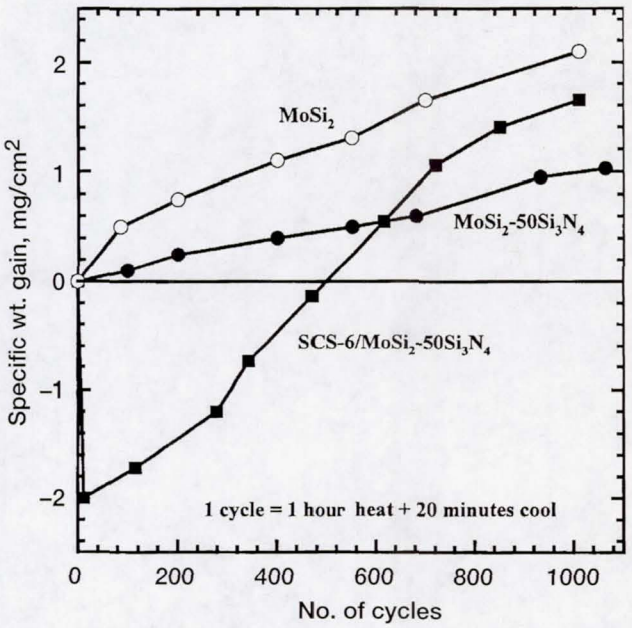
Specific wt. gain, mg/cm2
2
1
0
−1
−2
MoSi2
MoSi2-50Si3N4
SCS-6/MoSi2-50Si3N4
1 cycle = 1 hour heat + 20 minutes cool
0
200
400
600
800
1000
No. of cycles

Figure 5

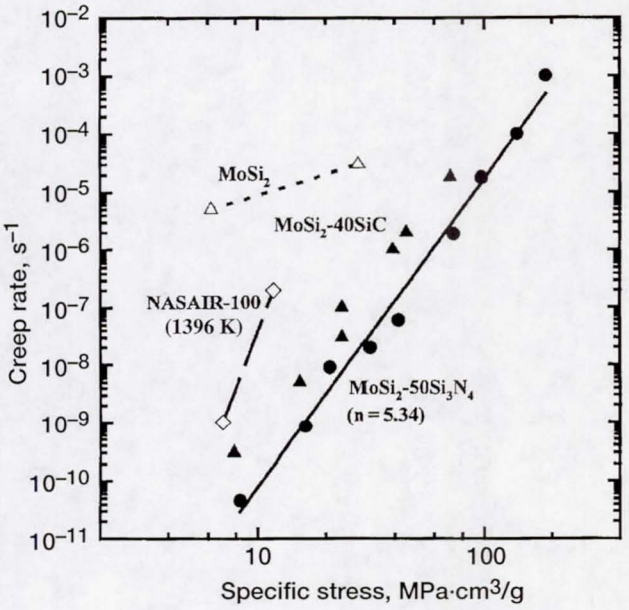
Creep rate, s$^{-1}$
$10^{-2}$
$10^{-3}$
$10^{-4}$
$10^{-5}$
$10^{-6}$
$10^{-7}$
$10^{-8}$
$10^{-9}$
$10^{-10}$
$10^{-11}$
MoSi$_2$
MoSi$_2$-40SiC
NASAIR-100
(1396 K)
MoSi$_2$-50Si$_3$N$_4$
(n = 5.34)
10
100
Specific stress, MPa·cm$^3$/g

Figure 6

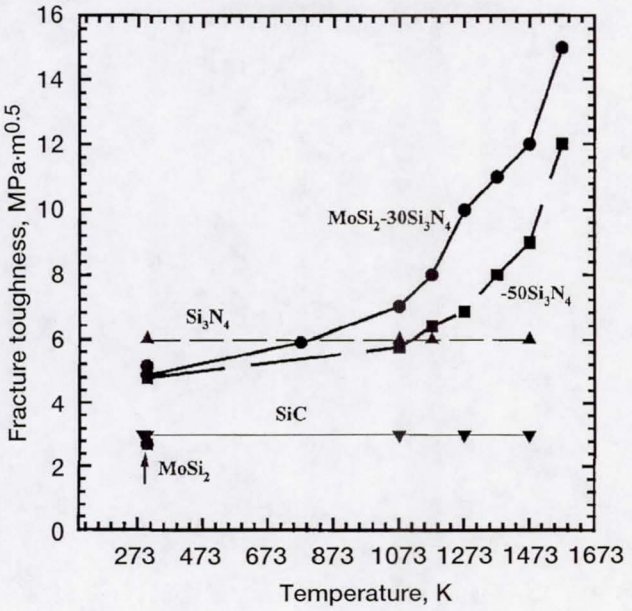
Fracture toughness, MPa·m$^{0.5}$
16
14
12
10
8
6
4
2
0
273
473
673
873
1073
1273
1473
1673
Temperature, K
$MoSi_2$-30$Si_3N_4$
-50$Si_3N_4$
$Si_3N_4$
SiC
$MoSi_2$

Figure 7

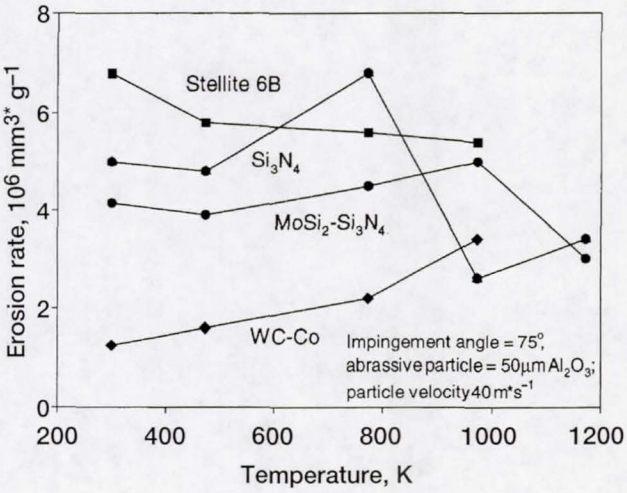
Erosion rate, $10^6$ mm$^3$* g$^{-1}$
Temperature, K
Stellite 6B
$Si_3N_4$
$MoSi_2$-$Si_3N_4$
WC-Co
Impingement angle = 75°,
abrassive particle = 50μm $Al_2O_3$;
particle velocity 40 m*s$^{-1}$
0
2
4
6
8
200
400
600
800
1000
1200

Figure 8

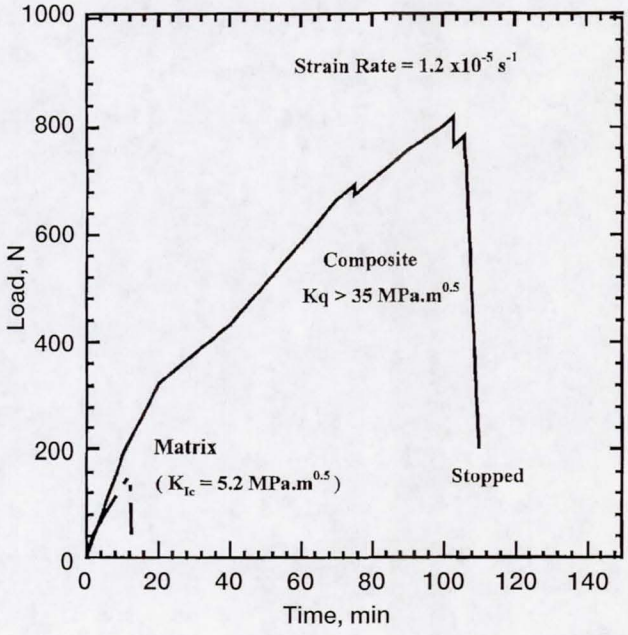
Strain Rate = 1.2 x10$^{-5}$ s$^{-1}$
Composite
Kq > 35 MPa.m$^{0.5}$
Matrix
( $K_{Ic}$ = 5.2 MPa.m$^{0.5}$ )
Stopped
Load, N
Time, min
0
200
400
600
800
1000
0
20
40
60
80
100
120
140

Figure 9

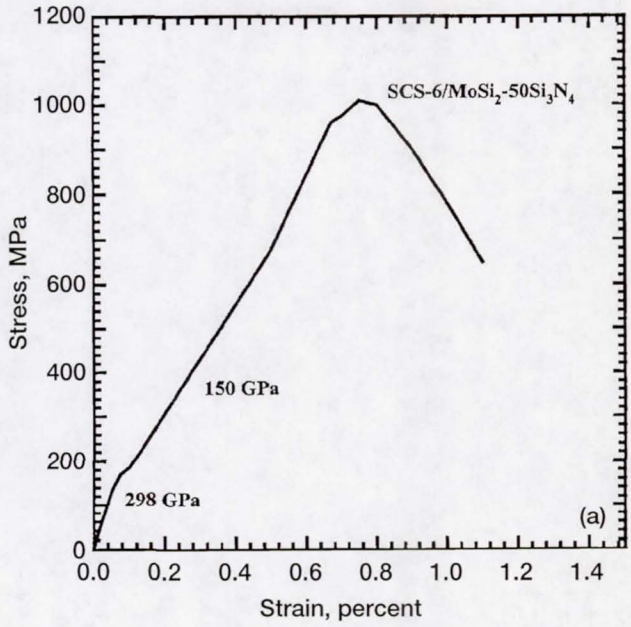
SCS-6/MoSi2-50Si3N4
150 GPa
298 GPa
(a)
Stress, MPa
Strain, percent
0
200
400
600
800
1000
1200
0.0
0.2
0.4
0.6
0.8
1.0
1.2
1.4

Figure 10a

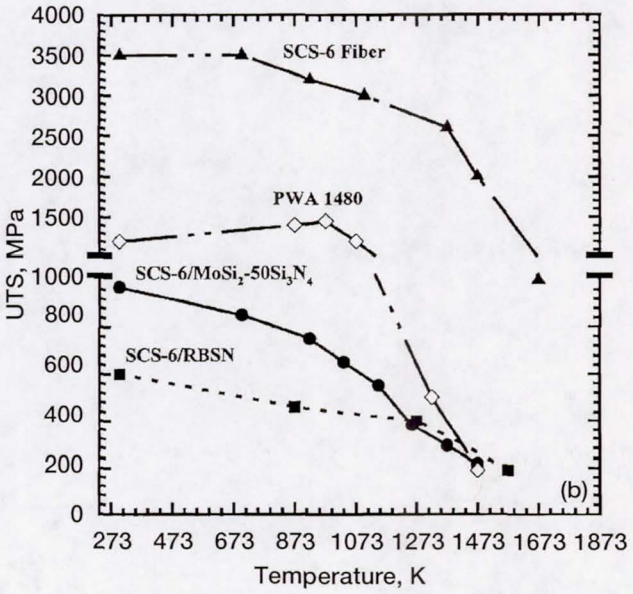
4000
3500
3000
2500
2000
1500
1000
800
600
400
200
0
UTS, MPa
SCS-6 Fiber
PWA 1480
SCS-6/MoSi2-50Si3N4
SCS-6/RBSN
(b)
273 473 673 873 1073 1273 1473 1673 1873
Temperature, K

Figure 10b

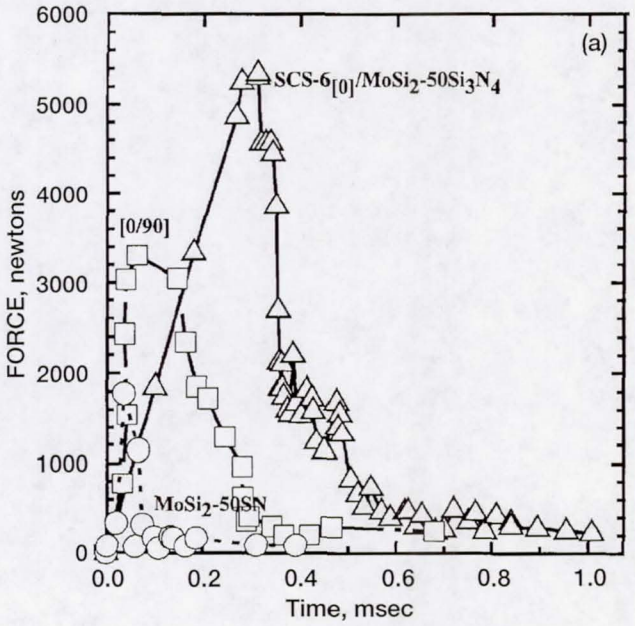
6000
5000
4000
3000
2000
1000
0
FORCE, newtons
0.0
0.2
0.4
0.6
0.8
1.0
Time, msec
(a)
SCS-6[0]/MoSi2-50Si3N4
[0/90]
MoSi2-50SN

Figure 11(a)

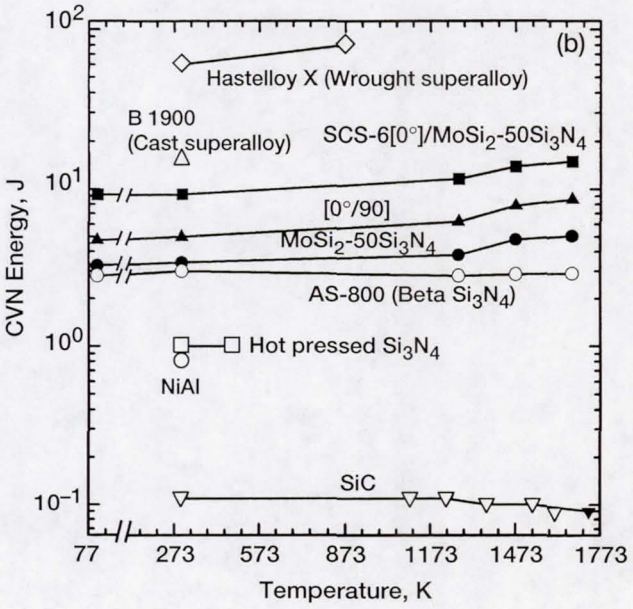
(b)
Hastelloy X (Wrought superalloy)
B 1900
(Cast superalloy)
SCS-6[0°]/MoSi2-50Si3N4
[0°/90]
MoSi2-50Si3N4
AS-800 (Beta Si3N4)
Hot pressed Si3N4
NiAl
SiC
CVN Energy, J
Temperature, K
10^2
10^1
10^0
10^-1
77
273
573
873
1173
1473
1773

Figure 11(b)

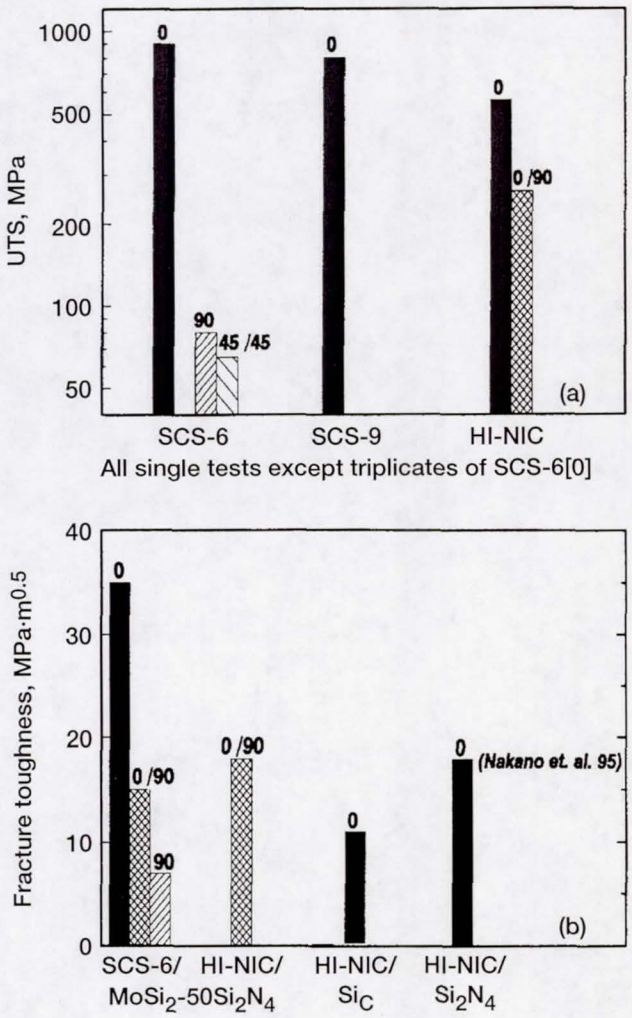
UTS, MPa
1000
500
200
100
50
0
0
0
0 /90
90
45 /45
(a)
SCS-6
SCS-9
HI-NIC
All single tests except triplicates of SCS-6[0]
Fracture toughness, MPa·m^0.5
40
30
20
10
0
0
0 /90
90
0 /90
0
0
(Nakano et. al. 95)
(b)
SCS-6/ MoSi2-50Si2N4
HI-NIC/ Si2N4
HI-NIC/ SiC
HI-NIC/ Si2N4

Figure 12

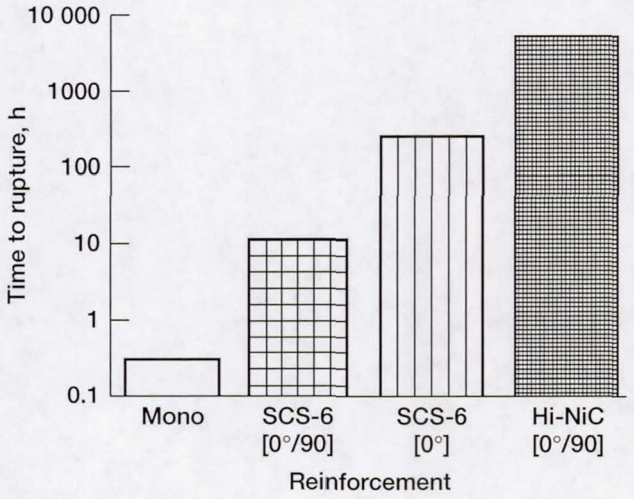
10 000
1000
100
10
1
0.1
Time to rupture, h
Mono
SCS-6
[0°/90]
SCS-6
[0°]
Hi-NiC
[0°/90]
Reinforcement

Figure 13

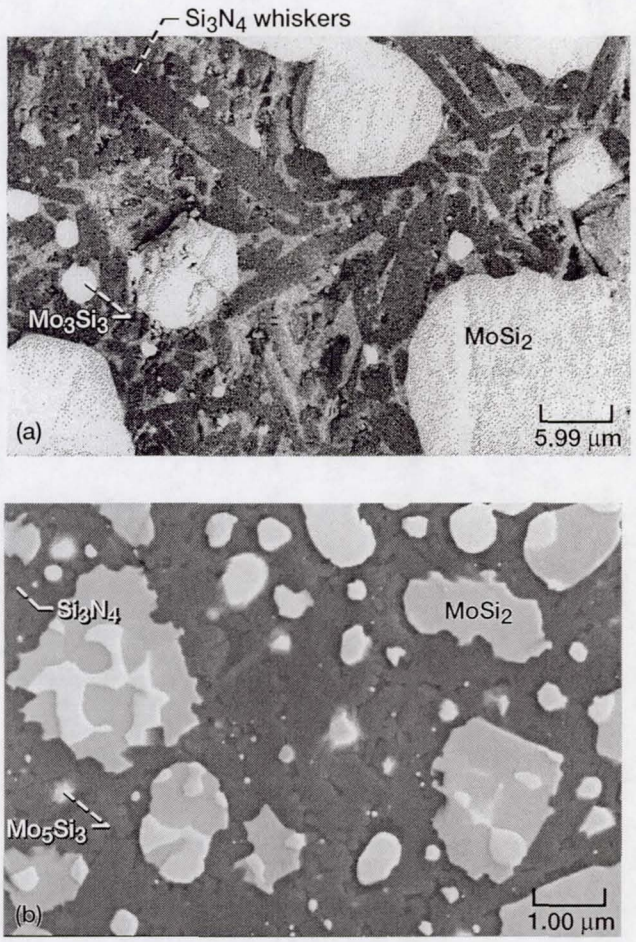
$Si_3N_4$ whiskers
$Mo_3Si_3$
$MoSi_2$
(a)
5.99 μm
$Si_3N_4$
$MoSi_2$
$Mo_5Si_3$
(b)
1.00 μm

Figure 14

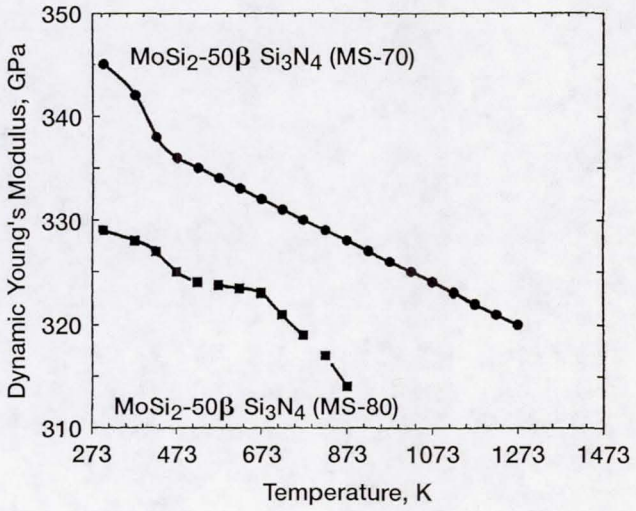
350
340
330
320
310
Dynamic Young's Modulus, GPa
MoSi2-50β Si3N4 (MS-70)
MoSi2-50β Si3N4 (MS-80)
273
473
673
873
1073
1273
1473
Temperature, K

Figure 15

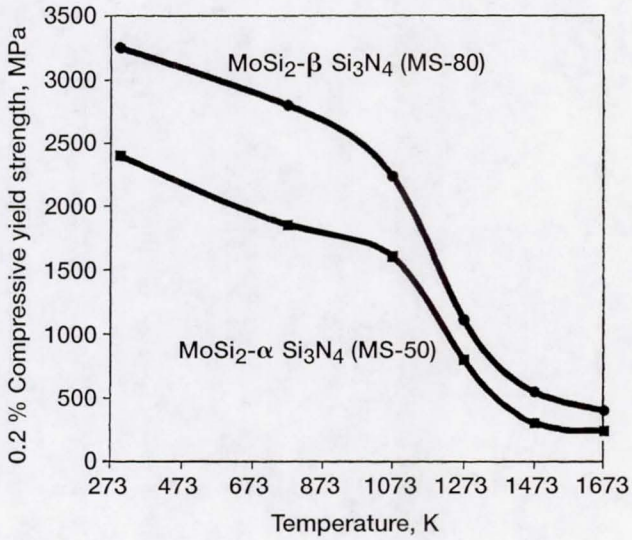
0.2 % Compressive yield strength, MPa
3500
3000
2500
2000
1500
1000
500
0
MoSi2-β Si3N4 (MS-80)
MoSi2-α Si3N4 (MS-50)
273
473
673
873
1073
1273
1473
1673
Temperature, K

Figure 16

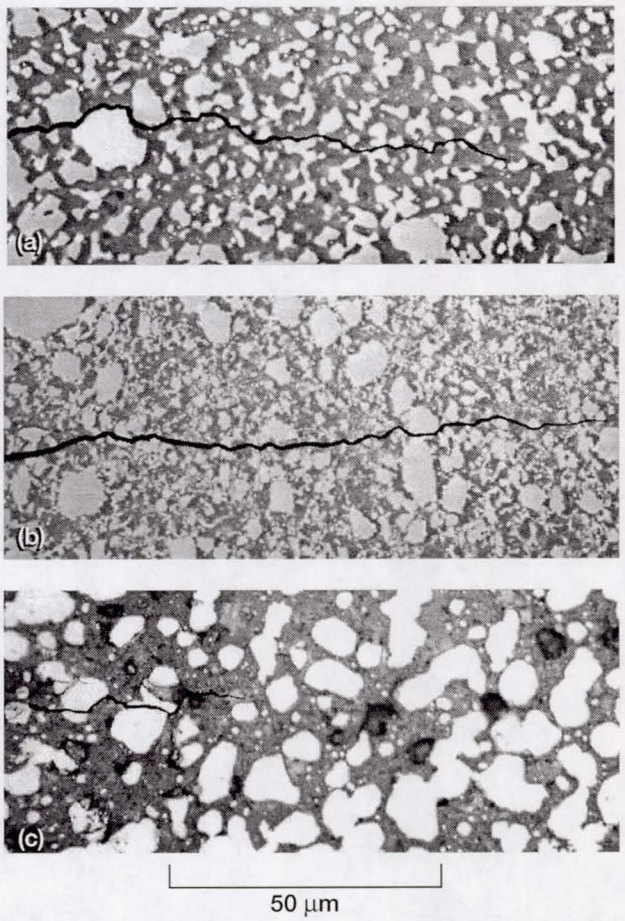


Figure 17

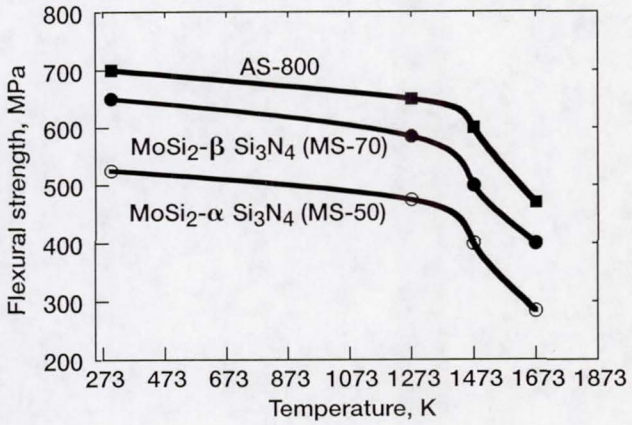
800
700
600
500
400
300
200
Flexural strength, MPa
AS-800
MoSi2-β Si3N4 (MS-70)
MoSi2-α Si3N4 (MS-50)
273 473 673 873 1073 1273 1473 1673 1873
Temperature, K

Figure 18

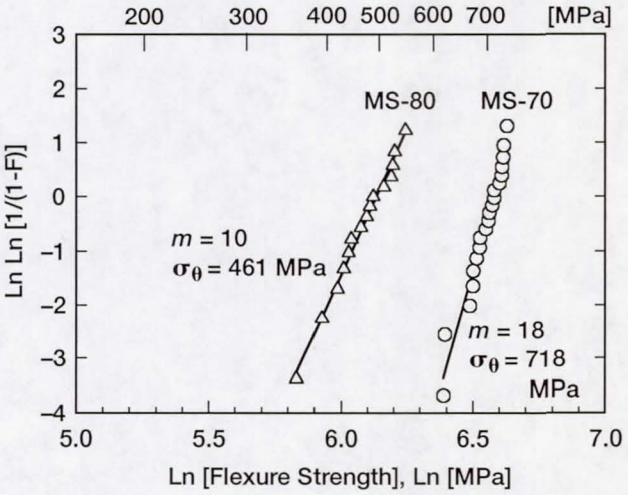
200
300
400
500
600
700
[MPa]
3
2
1
0
−1
−2
−3
−4
Ln Ln [1/(1-F)]
MS-80
MS-70
m = 10
σθ = 461 MPa
m = 18
σθ = 718
MPa
5.0
5.5
6.0
6.5
7.0
Ln [Flexure Strength], Ln [MPa]

Figure 19

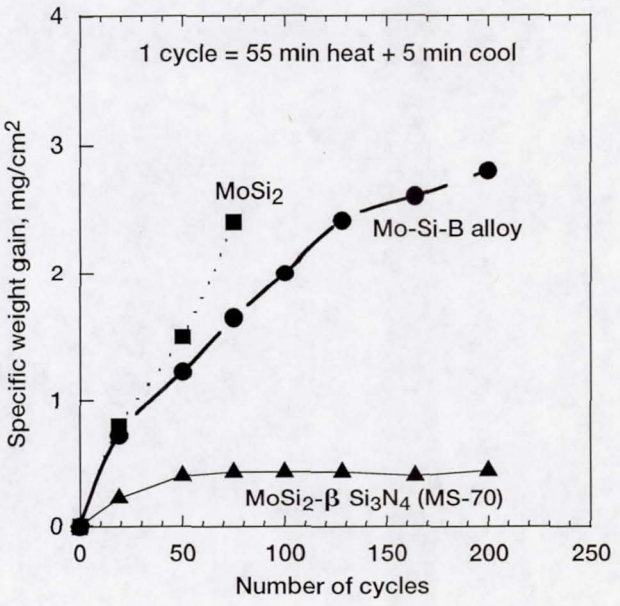
1 cycle = 55 min heat + 5 min cool
Specific weight gain, mg/cm2
MoSi2
Mo-Si-B alloy
MoSi2-β Si3N4 (MS-70)
Number of cycles
0
1
2
3
4
0
50
100
150
200
250

Figure 20